

Current Biology

Distributed chromatic processing at the interface between retina and brain in the larval zebrafish

Highlights

- Larval zebrafish show spectrally sensitive cells along their retinotectal projection
- Most AFs and central brain areas studied show spectrally selective responses
- Optic tectum separates stimuli with more reliability and stability than AF10 does
- This improvement stems from a more distributed spectral code in tectum versus AF10

Authors

Drago A. Guggiana Nilo,
Clemens Riegler, Mark Hübener,
Florian Engert

Correspondence

druggiana@neuro.mpg.de (D.A.G.N.),
florian@mcb.harvard.edu (F.E.)

In Brief

Guggiana Nilo et al. describe the spectral response characteristics of RGC terminals and many of their targets in the brain. They find that there is a wide array of spectral responses in most areas studied, and that optic tectum separates chromatic information more reliably than AF10 does, mostly due to a more distributed neural code.

Report

Distributed chromatic processing at the interface between retina and brain in the larval zebrafish

Drago A. Guggiana Nilo,^{1,2,3,5,6,*} Clemens Riegler,^{1,4} Mark Hübener,³ and Florian Engert^{1,*}

¹Department of Molecular and Cellular Biology, Harvard University, Cambridge, MA 02138, USA

²Harvard Biophysics Graduate Program, Harvard University, Boston, MA 02115, USA

³Department Synapses-Circuits-Plasticity, Max Planck Institute of Neurobiology, 81252 Martinsried, Germany

⁴Department of Neuroscience and Developmental Biology, University of Vienna, A-1090 Vienna, Austria

⁵Twitter: @drguggiana

⁶Lead contact

*Correspondence: drguggiana@neuro.mpg.de (D.A.G.N.), florian@mcb.harvard.edu (F.E.)

<https://doi.org/10.1016/j.cub.2021.01.088>

SUMMARY

Larval zebrafish (*Danio rerio*) are an ideal organism for studying color vision, as their retina possesses four types of cone photoreceptors, covering most of the visible range and into the UV.^{1,2} Additionally, their eye and nervous systems are accessible to imaging, given that they are naturally transparent.^{3–5} Recent studies have found that, through a set of wavelength-range-specific horizontal, bipolar, and retinal ganglion cells (RGCs),^{6–9} the eye relays tetrachromatic information to several retinorecipient areas (RAs).^{10–13} The main RA is the optic tectum, receiving 97% of the RGC axons via the neuropil mass termed arborization field 10 (AF10).^{14,15} Here, we aim to understand the processing of chromatic signals at the interface between RGCs and their major brain targets. We used 2-photon calcium imaging to separately measure the responses of RGCs and neurons in the brain to four different chromatic stimuli in awake animals. We find that chromatic information is widespread throughout the brain, with a large variety of responses among RGCs, and an even greater diversity in their targets. Specific combinations of response types are enriched in specific nuclei, but there is no single color processing structure. In the main interface in this pathway, the connection between AF10 and tectum, we observe key elements of neural processing, such as enhanced signal decorrelation and improved chromatic decoding.^{16,17} A richer stimulus set revealed that these enhancements occur in the context of a more distributed code in tectum, facilitating chromatic signal association in this small vertebrate brain.

RESULTS

Stimulation with different wavelengths evokes diverse responses in RGCs and central brain

Our goal was to characterize the processing of chromatic information from the fish's eye to the rest of the brain. For this, we utilized a custom 4-channel projector (365-, 397-, 463-, and 606-nm LEDs) synchronized to the scanning of a 2-photon microscope (Figures 1A and 1B). We showed four spectrally different, temporally oscillating full-field stimuli to the animal (Figure 1C). Their intensity and wavelength were selected to approximate the naturalistic spectrum larvae experience in the wild⁶ (Figure S1A). We genetically targeted the calcium indicator GCaMP6s¹⁸ to either the axonal terminals of retinal ganglion cells (RGCs) projecting from the eye to the different arborization fields (AFs), or a set of retinorecipient areas (RAs) in the dorsal brain (Figures 1D and S1E). We imaged one hemisphere for AFs and both for RAs. We stimulated the fish from below, as all four cone types are represented more evenly in the dorsal retina,^{6,8} and rods are not yet active at this developmental stage^(19,20); but see Venkatraman et al.²¹. This yielded a variety of calcium responses in both the RGCs and RAs (Figures 1E, 1F, and S1F–S1H).

As a first step, we wanted to describe the wavelength specificity of the regions of interest (ROIs). Using a linear model that takes into consideration the spectra of our stimuli and the zebrafish cones, we extracted the contribution (gain) of each cone type to the observed responses (Figure 1H).^{22,23} This confirmed earlier findings that blue gains are mostly negative (indicative of OFF responses) and that UV gains are typically higher than the rest.^{6,8,24–27} We used these gains to define spectral polarities for both populations (Figures 1I, S1B, and S1C). There was a higher diversity of polarities in RAs compared to RGCs, although most RGCs matched the RA patterns, and most polarities were polychromatic.

Do different wavelength ranges map to particular brain regions? To test this, we compared the spatial activation patterns elicited in both populations via registration of all imaging volumes to a reference brain (Figure 1G).²⁸ Each stimulus elicited only partially overlapping activation patterns, both in the antero-posterior as well as in the dorso-ventral axis (Figures 1J and S1D). Furthermore, the RGC and RA patterns show a weak wavelength-dependent gradient from the posterior to the anterior visual field based on tectal retinotopy.²⁹ 3D quantification of these patterns revealed that the UV pattern is the most unique,

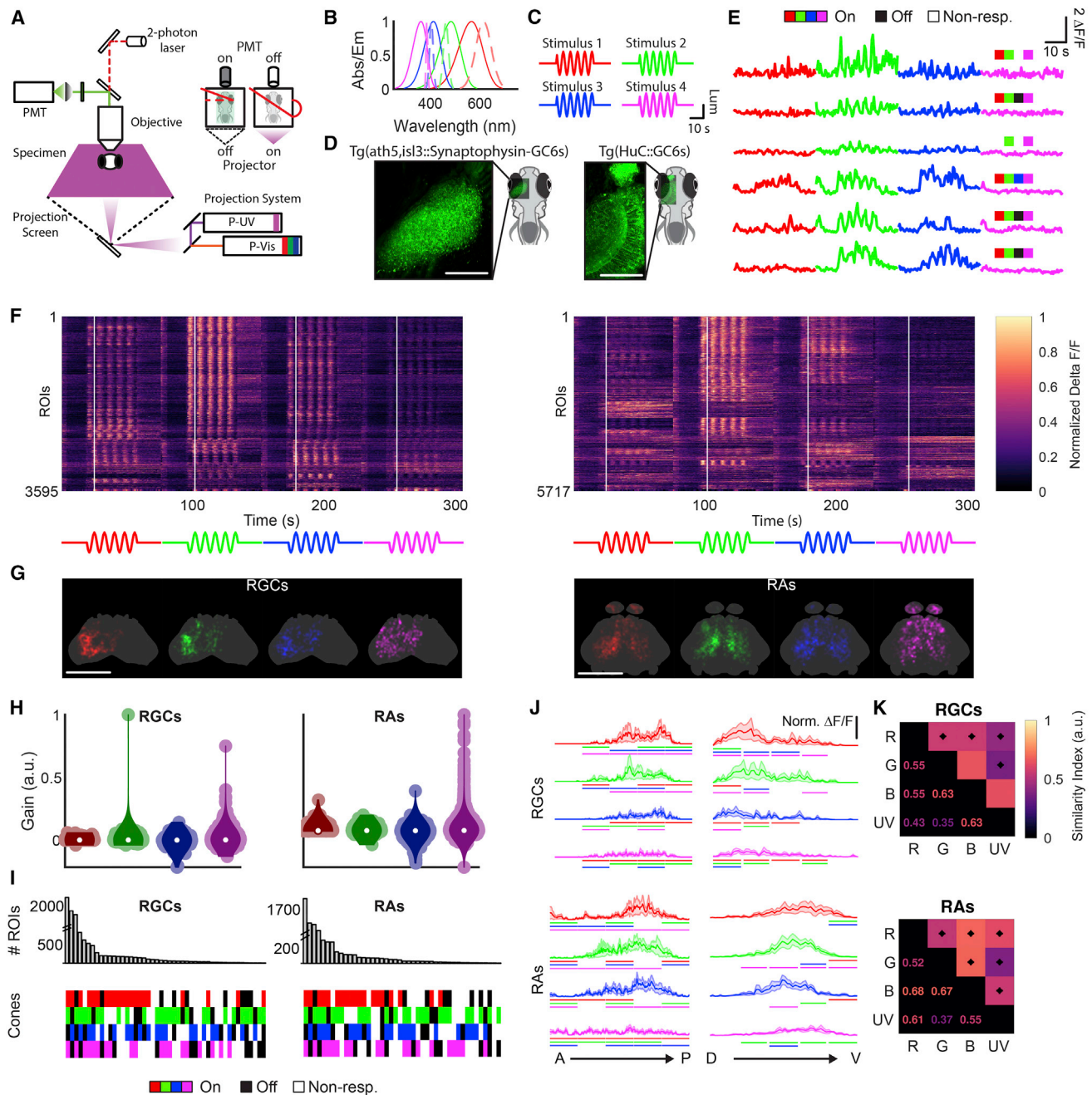


Figure 1. Stimulation with different wavelengths evokes a variety of responses in zebrafish RGCs and central brain

(A) Schematic of the setup used for stimulation, projecting chromatic stimuli from the bottom using a custom-designed projector with four channels. The inset illustrates alternation between stimulation and recording over the mirror turning cycle.

(B) Absorption spectra of the zebrafish cones (solid lines) and emission spectra of the LEDs (dotted lines) used in the projector.

(C) Full-field, temporally sinusoidal stimuli.

(D) Average images from the *isl3/ath5:GCaMP6s* and *HuC:GCaMP6s* lines used to label RGCs and RAs, respectively. Scale bars, 100 μm .

(E) Representative $\Delta F/F$ responses to all four stimuli from RGCs and RAs. Indicated in each trace is the spectral type from (I).

(F) Full datasets for RGCs and RAs, with intensity reflecting the row-normalized $\Delta F/F$, sorted according to clusters depicted in Figure 2. White lines indicate first stimulus peak.

(G) Registered and interpolated anatomical maps of the regions of interest (ROIs), colored by preferred stimulus (see STAR Methods). Scale bars, 100 μm .

(H) Calculated gains for each cone from each ROI in RGCs and RAs.

(I) Spectral types obtained from categorizing the cone gains from both RGCs and RAs (bottom) and their counts (top).

(legend continued on next page)

although almost all patterns appeared to show more heterogeneity than suggested from the rather homogeneous cone layout in the dorsal retina (Figure 1K).^{6,8,14,30}

Chromatic responses cluster functionally and anatomically

Given the divergence of the spatial activation patterns elicited by each stimulus, we next tested whether the different calcium responses we observed (Figures 1F, S2A, and S2B) also displayed specific anatomical patterns (Figures 2A and 2B). To this end, we clustered these responses based on their spectro-temporal features. This analysis yielded 11 RGC clusters and 19 RA clusters, which displayed varying patterns of region specificity and spectro-temporal waveforms across fish (Figures 2C, 2D, and S2D–S2I). In RGCs, responses that followed the temporal structure of the stimulus were more common, whereas in RAs many clusters displayed sustained responses (e.g., cluster RA3) or responses that evolved over time (e.g., cluster RA17). In both populations, there was a dominant cluster that was present in almost all regions (clusters RGC1 and RA1), and that could be due to the interaction between our stimulus and the previously described coarse retinal spectral tuning.²⁷

Does spectral distribution of response types influence local wavelength processing? To assess this, we used a support vector machine (SVM) classifier to identify the stimulus. This showed that all four stimuli were separable across regions but with region-specific differences in performance, especially for the green and blue stimuli (Figures 2E and S2J). We corroborated this via a regression approach, where the clusters from each region were used to regress the clusters of another (Figure S2C). This showed, as expected, that AF10, the AF that terminates in tectum, carries information common to most AFs. Instead, other AFs showed more specific patterns, as predicted by connectivity.¹⁴ In RAs, all regions performed well, although cerebellum and habenula displayed more diverging patterns, even compared to tectum. Overall, RAs performed better at spectral classification than RGCs—especially in middle wavelengths that have more overlap—whereas RGCs performed better at intensity classification (Figure S2K). Hence, chromatic information is widespread in the larval brain, but with regional differences in the particular response types available.

Chromatic stimuli are better separated in tectum than in AF10

AF10 and tectum represent subsequent stages in the visual pathway,¹⁵ but tectum outperforms AF10 in stimulus separation (Figure 2E), even though there is chromatic processing already in the retina.^{8,27} Thus, tectum does not merely relay AF10 signals but contributes to chromatic processing. We therefore set out to uncover the nature of these computations (Figures 3A and 3B). First, we quantified the number of responsive ROIs for each combination of stimuli, given more wavelength-selective ROIs could result in better wavelength separation (Figure 3C).

We observed no significant difference between AF10 and tectum at this level, nor when we utilized the cone contributions instead (Figures S3C and S3D). Because sensory processing is often associated with enhanced decorrelation,¹⁶ we next quantified the decorrelation between the responses elicited by each pair of stimuli in both areas (Figure 3D). Decorrelation in tectum was higher than in AF10, but only by a small margin. It is noteworthy that limiting this analysis to the clusters in each area widened this decorrelation difference (Figure 3E).

But how does decorrelation translate into processing? We used principal-component analysis (PCA) to visualize the population-level activity time course during each stimulus, and aligned spaces across animals using canonical component analysis (CCA³¹; Figures 3F, S3E, and S3F). This showed that, whereas in AF10 there is only one main separation axis, in tectum the trajectories separate in all three dimensions, suggesting a higher-dimensional representation of chromatic stimuli. This was corroborated by calculating the normalized distances between the stimulus trajectories in PC space (Figure 3G). Therefore, tectum shows signatures of higher dimensionality, which supports the better stimulus separation in comparison to AF10.

Based on the clear separation of the PC trajectories in tectum, we hypothesized that, aside from gained dimensionality, this separation led to a more robust code. We confirmed this by visualizing the performance of an SVM classifier over the time course of the stimulus presentation (Figures 3H and 3I; see also Figures S3A and S3B). Indeed, whereas AF10 tends to fluctuate with the stimulus, the tectal performance was impervious to stimulus intensity changes. This stability could be mediated by several factors, one of which is how distributed information is across ROIs: a more distributed code would mean that the population response is less sensitive to single ROI fluctuations at any given moment. To assess this, we trained a classifier with increasing numbers of ROIs (Figure 3J), added by their importance to the classifier.³² Although tectum outperformed AF10 at every ROI number, it did so more pronouncedly at low numbers, pointing to a more distributed code for spectral information in tectum.

Wavelength separation extends to different spatiotemporal stimulus patterns

RGCs carry combined signals,⁸ and thus we wondered whether tectal chromatic processing involves separation of spectral signals from other submodalities. To answer this, we presented fish with patterns including local contrast, motion, or fast dynamics, both in red and UV (to maximally separate the cones activated by the stimuli) (Figures 4A and 4B). As with the previous stimulus set, we observed a large diversity of responses to the stimuli, both in terms of pattern and wavelength (Figures 4C and S4A–S4C). Registration into a reference brain confirms this heterogeneity, although the AF10 patterns appear more homogeneous (Figures 4D and 4E). In AF10, only the flash patterns show instances of divergence. Instead, in tectum, the diverging patterns are more numerous and distributed. How stimulus specific are

(J) Antero-posterior (left) and dorso-ventral (right) normalized calcium response profiles for RGCs (top) and RAs (bottom) for each stimulus. Lines denote $p < 0.05$ for difference between the region of the profile covered by the line and the corresponding region in the profile indicated by the line's color, Wilcoxon signed rank. (K) Spatial similarity of the response patterns elicited by the four stimuli. A star denotes overlap significantly different from monochromatic inter-trial overlap, Wilcoxon signed rank, $p < 0.05$. $n = 6$ animals and 3,595 ROIs for the RGC data; $n = 6$ animals and 5,717 ROIs for the RA data. See also Figure S1.

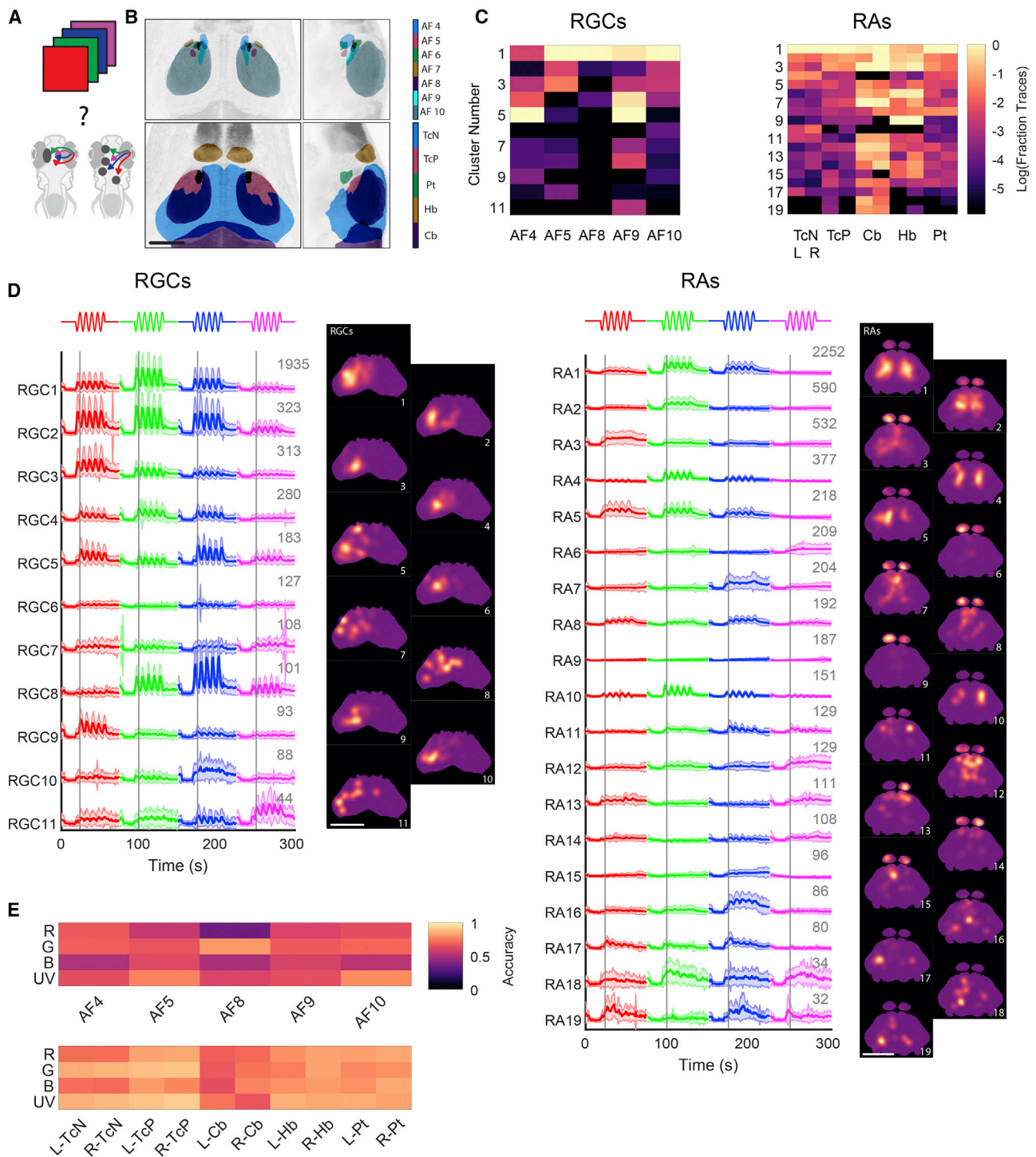


Figure 2. Chromatic responses cluster functionally and anatomically

(A) We presented four chromatic stimuli and measured responses from a number of brain regions to identify wavelength-sensitive areas.

(B) Anatomical location of the brain regions imaged for the RGC and RA populations. Scale bar, 100 μ m.

(C) Relative proportion of each cluster found in each of the brain regions imaged (normalized per brain region, plotted as log base 10).

(D) Average responses for each cluster, for RGCs (left) and RAs (right). Gray numbers indicate ROI numbers. Maps next to each cluster depict the average location of its ROIs. Gray lines indicate first stimulus peak. Scale bars, 100 μ m.

(E) Classification accuracy of an SVM classifier trained to discriminate between the stimuli for each region. Top: RGCs; bottom: RAs. AF, arborization field; R- and L-: right and left hemisphere; TcN, tectal neuropil region; TcP, tectal periventricular region; Cb, cerebellum; Hb, habenula; Pt, prepectum.

See also [Figure S2](#).

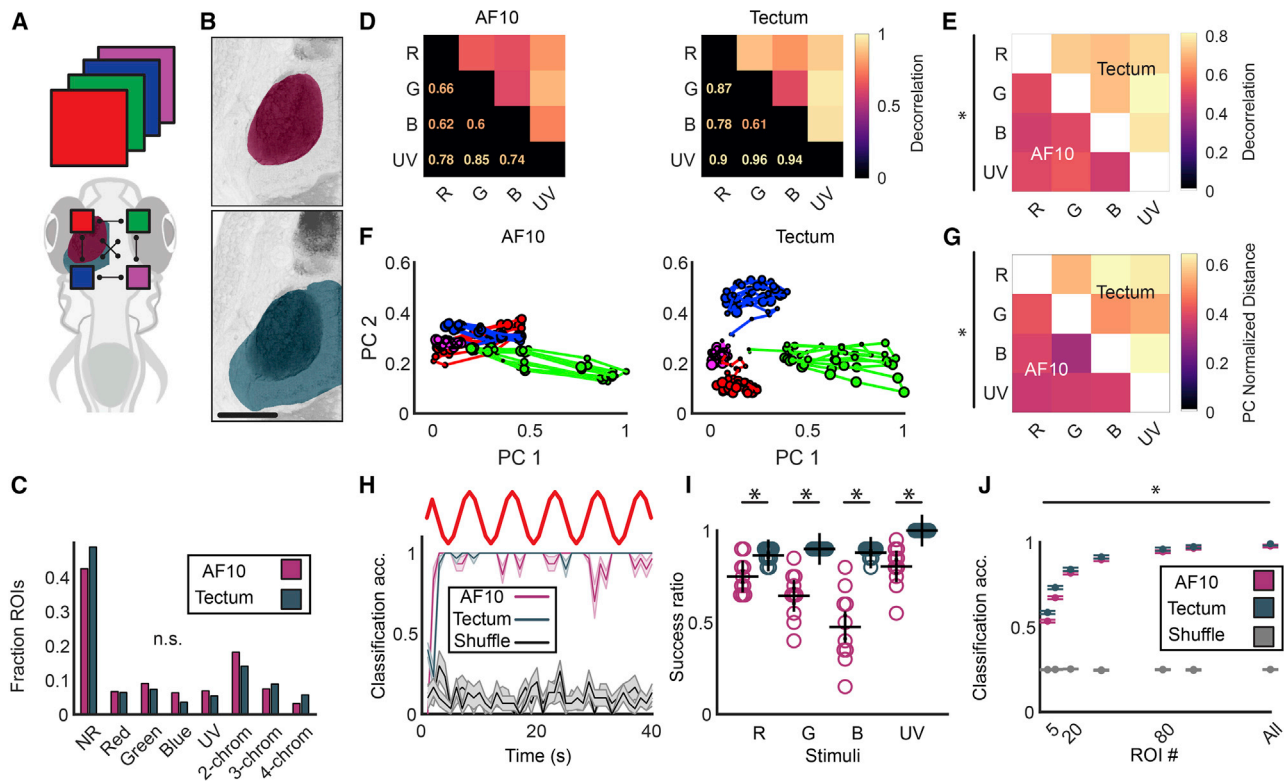


Figure 3. Chromatic stimuli are better separated in tectum than in AF10

(A) Comparison of the chromatic computations occurring between AF10 and tectum.
 (B) Anatomical layout of AF10 (top) and ipsilateral tectum (bottom). Scale bar, 100 μ m.
 (C) Histogram quantifying the number of ROIs assigned to the top 75th percentile of each stimulus, no stimulus (NR, non-responsive), or multiple stimuli for both populations. $p > 0.05$ for all bins tested separately, Wilcoxon signed rank.
 (D) Overall decorrelation of the neural activity evoked by each stimulus for both datasets.
 (E) Cluster average decorrelation for all pairs of stimuli for AF10 (below diagonal) and tectum (above diagonal). The deltas were evaluated pairwise; $p < 0.05$, Wilcoxon rank sum for all squares.
 (F) CCA-aligned and averaged PC trajectories over the course of the stimulation period for AF10 and tectum. Line color indicates stimulus, with dot size increasing over time.
 (G) Average pairwise Euclidean distances between the centroids of the point clouds corresponding to each stimulus response in PC space for AF10 and tectum after alignment. * $p < 0.05$, Wilcoxon rank sum performed pairwise.
 (H) Example SVM-based classification performance over time for AF10 and tectum compared to shuffle. Stimulus is on top.
 (I) Success ratio for classification of each stimulus in AF10 compared to tectum. * $p < 0.05$, Wilcoxon rank sum.
 (J) Classification performance for different ROI numbers, with an average of 10 repetitions for both populations and shuffles. * $p < 0.05$ Wilcoxon rank sum performed pairwise.
 (A–E, H, and I) $n = 6$ animals and 1,776 ROIs for tectum; $n = 6$ animals and 2,670 ROIs for AF10.
 (F and G) $n = 3$ animals and 1,604 ROIs for tectum; $n = 5$ animals and 1,313 ROIs for AF10.
 See also [Figure S3](#).

the ROIs? To address this question, we grouped the responsive ROIs based on their preferred pattern and wavelength (Figures 4F and S4D). We found multiple types, but the distribution was broader for tectum than for AF10, supporting the improved decorrelation we observed.

But does the more distributed tectal code also play a role in pattern processing? To answer this, we repeated the neuron addition analysis (Figure 4G). It is noteworthy that, taking all AF10 responses into account, they outperform tectum but smaller numbers do not. This further supports the idea of a distributed code in tectum, whereas the AF10 code seems to be more local. To further disentangle the intricacies of this computation, we trained separate classifiers for the pattern or

the spectral component of the stimuli. Whereas the pattern classifier shows similar accuracy throughout for both populations, the chromatic classifier follows the results observed in Figure 3. Hence, there is a clear chromatic processing improvement in tectum compared to AF10, even in the presence of other modalities, mediated by better pattern decorrelation, stability, and a more distributed code.

DISCUSSION

In this work, we show how chromatic stimuli are processed in two successive stages of the larval zebrafish visual pathway. We found that chromatic information coming from below is

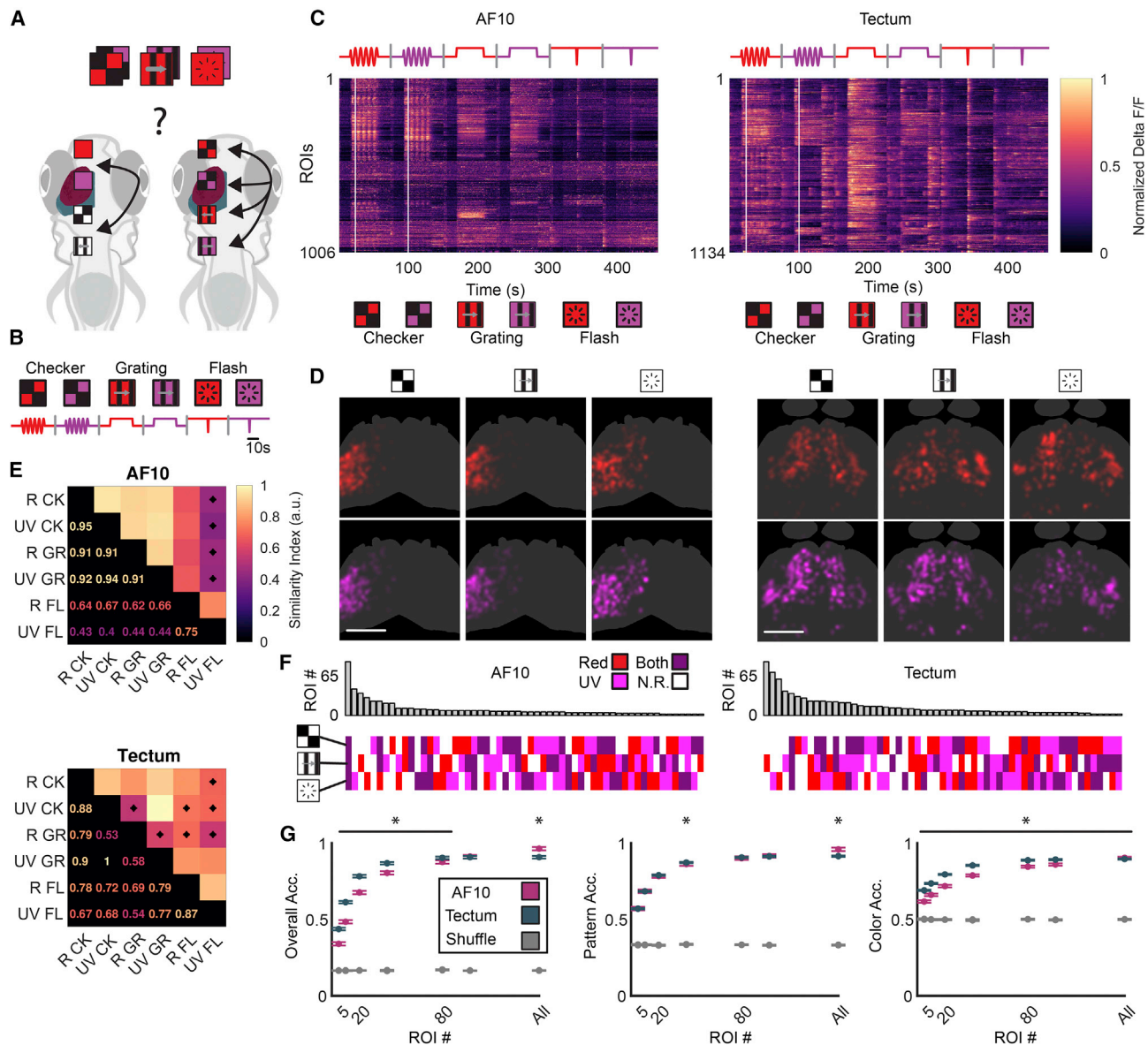


Figure 4. Wavelength separation extends to different spatiotemporal patterns

(A) Red or UV stimuli were utilized to assess whether different spatiotemporal patterns affect wavelength processing between AF10 and tectum.

(B) Schematic of the stimuli, combining spatiotemporal patterns with red and UV.

(C) Trial-averaged fluorescence traces. Intensity is row-normalized fluorescence. Traces were sorted via hierarchical clustering for display. White lines show the first peak of the checkerboard oscillation.

(D) Anatomical interpolated ROI distribution from AF10 (left) and tectum (right), depicted according to the stimulus that elicited the maximum response for that ROI. Scale bars, 100 μ m.

(E) Anatomical similarity matrix for the response patterns elicited by each stimulus. A star denotes overlap significantly different from inter-trial overlap, Wilcoxon signed rank, $p < 0.05$.

(F) Breakdown of the spectral/pattern types for both populations. Top: count of ROIs of each type. Bottom: spectral and pattern selectivity for that type.

(G) ROI addition analysis as described for Figure 3J. Left: classifier trained to separate all 6 stimuli. Middle: classifier trained to separate only patterns and disregard wavelength. Right: classifier trained to separate only wavelength and disregard patterns. * $p < 0.05$, Wilcoxon rank sum performed pairwise.

$n = 4$ animals and 1,006 ROIs for AF10; $n = 11$ animals and 1,134 ROIs for tectum. CK, checkerboard; GR, moving grating; FL, dark flash.

See also Figure S4.

widely available across the larval brain, even in cerebellum and habenula, structures not usually associated with chromatic processing^(33–35), but see Lin and Jesuthasan⁽³⁶⁾ and Dreosti et al.⁽³⁷⁾,

whereas it is absent from others, such as AF6 and AF7. When focusing on AF10 and the optic tectum, we observed that the chromatic computations are more advanced in tectum, as

evidenced by improved decoding and better pattern decorrelation and stability. Finally, by comparing the responses to different behaviorally relevant stimuli,^{38–41} we confirmed that tectum utilizes a more distributed neural code than AF10, allowing it to better separate chromatic information from the RGC inputs.

Recently, Zhou, Bear et al.⁸ described the spectral properties of RGC dendrites and somata in the eye of the larval zebrafish. Our results corroborate their finding of mostly OFF blue weights and high UV weights in RGCs, and also of simple and complex color opponencies, including partial matching to the types they find in the dorsal retina (Figure S1B). Additionally, our results are also in agreement with recent findings describing the coarse spectral tuning of the larval eye as RG ON, B OFF, and UV ON.^{12,27} Interestingly, Zhou, Bear et al. also describe the presence of a time code in RGC responses. Due to our imaging protocol, we are unable to resolve the calcium dynamics at the rates this time code is observed (although see Figures S1C and S2I), but in future studies it will be interesting to elucidate the interaction between the slower time component we observe with the described RGC time code and chromatic processing.

How do chromatic circuits arise in light of our results? Based on what is known about tectal connectivity,^{42,43} aside from sensory inputs, there is also a large amount of intratectal circuitry that most likely has a pivotal role in the computations we describe. Neurons with refined chromatic responses could arise by combining like-tuned RGC terminals. The resulting neurons would then have a more stable output than individual RGC terminals, and their connections to other like tectal neurons would allow the entire network to improve in decorrelating the chromatic signals, consistent with the distributed code we observed. Such a circuit motif has been described for systems like the larval olfactory system, where decorrelation is essential for decoupling inputs.¹⁶ This circuit structure would also be compatible with some of the previously described wavelength-dependent behaviors in the larva, such as prey capture,⁹ blue vertical migration,³⁶ UV avoidance,⁴⁴ and the optomotor response in red-green.⁴⁵ In agreement with this, we observed that the broad spatial organization of chromatic signals deviates beyond the retinotopic expectation, allowing for development of pathways supporting specific submodalities of chromatic vision as the ones mentioned above.

Finally, in mammals, and in particular in primates, chromatic information follows a processing path down the temporal stream, a succession of cortical areas involved in object recognition. These comprise from V1 to V2 and V4.^{46,47} In the latter, one finds neural correlates of more complex aspects, such as hue. We found no obvious color processing centers in the fish brain, as spectral responses appear anatomically distributed, but more research is warranted in uncovering the full color vision pathway in the larval brain.

STAR★METHODS

Detailed methods are provided in the online version of this paper and include the following:

- KEY RESOURCES TABLE
- RESOURCE AVAILABILITY
 - Lead contact

- Materials availability
- Data and code availability
- EXPERIMENTAL MODEL AND SUBJECT DETAILS
 - Zebrafish
- METHOD DETAILS
 - Stimulus presentation
 - Brain imaging
 - Data pre-processing
 - Calculation of cone gains
 - Gain pattern classification
 - Registration
 - Similarity index
 - Dimensionality reduction and clustering
 - UMAP
 - SVM color and intensity classification
 - ROI addition analysis
 - Success ratio
 - Cluster to cluster regression
 - Correlation analysis
 - PCA-CCA
 - Convolution of chromatic kernels
- QUANTIFICATION AND STATISTICAL ANALYSIS

SUPPLEMENTAL INFORMATION

Supplemental Information can be found online at <https://doi.org/10.1016/j.cub.2021.01.088>.

ACKNOWLEDGMENTS

The authors would like to thank Martin Haesemeyer, Owen Randlett, and Tom Baden for their contributions to data analysis, and Iris Odstrcil, Joseph Donovan, and Armin Bahl for helpful comments on the manuscript. Funding was received from the National Institutes of Health (U19NS104653, R43 OD024879) and the Simons Foundation (SCGB 542973).

AUTHOR CONTRIBUTIONS

D.A.G.N. conceived the project with the help of F.E.; D.A.G.N. conducted the experiments and analyzed the data; C.R. provided the fish strains used and advised on experiment execution; F.E. advised on experiments and data analysis; D.A.G.N., with the help of M.H., wrote the manuscript; D.A.G.N., M.H., C.R., and F.E. edited the manuscript.

DECLARATION OF INTERESTS

The authors declare no competing interests.

Received: July 9, 2020

Revised: December 30, 2020

Accepted: January 25, 2021

Published: February 25, 2021

REFERENCES

1. Raymond, P.A., Barthel, L.K., and Curran, G.A. (1995). Developmental patterning of rod and cone photoreceptors in embryonic zebrafish. *J. Comp. Neurol.* 359, 537–550.
2. Robinson, J., Schmitt, E.A., Hárosi, F.I., Reece, R.J., and Dowling, J.E. (1993). Zebrafish ultraviolet visual pigment: absorption spectrum, sequence, and localization. *Proc. Natl. Acad. Sci. USA* 90, 6009–6012.
3. Spence, R., Gerlach, G., Lawrence, C., and Smith, C. (2008). The behaviour and ecology of the zebrafish, *Danio rerio*. *Biol. Rev. Camb. Philos. Soc.* 83, 13–34.

4. Portugues, R., Feierstein, C.E., Engert, F., and Orger, M.B. (2014). Whole-brain activity maps reveal stereotyped, distributed networks for visuomotor behavior. *Neuron* *81*, 1328–1343.
5. Ahrens, M.B., Orger, M.B., Robson, D.N., Li, J.M., and Keller, P.J. (2013). Whole-brain functional imaging at cellular resolution using light-sheet microscopy. *Nat. Methods* *10*, 413–420.
6. Zimmermann, M.J.Y., Nevala, N.E., Yoshimatsu, T., Osorio, D., Nilsson, D.-E., Berens, P., and Baden, T. (2018). Zebrafish differentially process colour across visual space to match natural scenes. *Curr. Biol.* *28*, 2018–2032.e5.
7. Connaughton, V.P., and Nelson, R. (2010). Spectral responses in zebrafish horizontal cells include a tetraphasic response and a novel UV-dominated triphasic response. *J. Neurophysiol.* *104*, 2407–2422.
8. Zhou, M., Bear, J., Roberts, P.A., Janiak, F.K., Semmelhack, J., Yoshimatsu, T., and Baden, T. (2020). Zebrafish retinal ganglion cells asymmetrically encode spectral and temporal information across visual space. *Curr. Biol.* *30*, 2927–2942.e7.
9. Yoshimatsu, T., Schröder, C., Nevala, N.E., Berens, P., and Baden, T. (2020). Fovea-like photoreceptor specializations underlie single UV cone driven prey-capture behavior in zebrafish. *Neuron* *107*, 320–337.e6.
10. Ma, M., Kler, S., and Pan, Y.A. (2020). Structural neural connectivity analysis in zebrafish with restricted anterograde transneuronal viral labeling and quantitative brain mapping. *Front. Neural Circuits* *13*, 85.
11. Wulliman, M.F., Rupp, B., and Reichert, H. (2012). *Neuroanatomy of the Zebrafish Brain: A Topological Atlas* (Birkhäuser).
12. Bartel, P., Janiak, F.K., Osorio, D., and Baden, T. (2020). Colourfulness as a possible measure of object proximity in the larval zebrafish brain. [bioRxiv. https://doi.org/10.1101/2020.12.03.410241](https://doi.org/10.1101/2020.12.03.410241).
13. Fornetto, C., Tiso, N., Pavone, F.S., and Vanzi, F. (2020). Colored visual stimuli evoke spectrally tuned neuronal responses across the central nervous system of zebrafish larvae. *BMC Biol.* *18*, 172.
14. Robles, E., Laurell, E., and Baier, H. (2014). The retinal projectome reveals brain-area-specific visual representations generated by ganglion cell diversity. *Curr. Biol.* *24*, 2085–2096.
15. Burrill, J.D., and Easter, S.S., Jr. (1994). Development of the retinofugal projections in the embryonic and larval zebrafish (*Brachydanio rerio*). *J. Comp. Neurol.* *346*, 583–600.
16. Niessing, J., and Friedrich, R.W. (2010). Olfactory pattern classification by discrete neuronal network states. *Nature* *465*, 47–52.
17. Johnson, K.O. (2000). Neural coding. *Neuron* *26*, 563–566.
18. Chen, T.-W., Wardill, T.J., Sun, Y., Pulver, S.R., Renninger, S.L., Baohan, A., Schreier, E.R., Kerr, R.A., Orger, M.B., Jayaraman, V., et al. (2013). Ultrasensitive fluorescent proteins for imaging neuronal activity. *Nature* *499*, 295–300.
19. Branchek, T., and Bremiller, R. (1984). The development of photoreceptors in the zebrafish, *Brachydanio rerio*. I. Structure. *J. Comp. Neurol.* *224*, 107–115.
20. Bilotta, J., Saszik, S., and Sutherland, S.E. (2001). Rod contributions to the electroretinogram of the dark-adapted developing zebrafish. *Dev. Dyn.* *222*, 564–570.
21. Venkatraman, P., Mills-Henry, I., Padmanabhan, K.R., Pascuzzi, P., Hassan, M., Zhang, J., Zhang, X., Ma, P., Pang, C.P., Dowling, J.E., et al. (2020). Rods contribute to visual behavior in larval zebrafish. *Invest. Ophthalmol. Vis. Sci.* *61*, 11.
22. Estévez, O., and Spekreijse, H. (1982). The “silent substitution” method in visual research. *Vision Res.* *22*, 681–691.
23. Mitchell, D.E., and Rushton, W.A. (1971). Visual pigments in dichromats. *Vision Res.* *11*, 1033–1043.
24. Risner, M.L., Lemerise, E., Vukmanic, E.V., and Moore, A. (2006). Behavioral spectral sensitivity of the zebrafish (*Danio rerio*). *Vision Res.* *46*, 2625–2635.
25. McDowell, A.L., Dixon, L.J., Houchins, J.D., and Bilotta, J. (2004). Visual processing of the zebrafish optic tectum before and after optic nerve damage. *Vis. Neurosci.* *21*, 97–106.
26. Cameron, D.A. (2002). Mapping absorbance spectra, cone fractions, and neuronal mechanisms to photopic spectral sensitivity in the zebrafish. *Vis. Neurosci.* *19*, 365–372.
27. Yoshimatsu, T., Bartel, P., Schröder, C., Janiak, F.K., St-Pierre, F., Berens, P., and Baden, T. (2020). Near-optimal rotation of colour space by zebrafish cones *in vivo*. [bioRxiv. https://doi.org/10.1101/2020.10.26.356089](https://doi.org/10.1101/2020.10.26.356089).
28. Randlett, O., Wee, C.L., Naumann, E.A., Nnaemeka, O., Schoppik, D., Fitzgerald, J.E., Portugues, R., Lacoste, A.M.B., Riegler, C., Engert, F., and Schier, A.F. (2015). Whole-brain activity mapping onto a zebrafish brain atlas. *Nat. Methods* *12*, 1039–1046.
29. Baier, H., Klostermann, S., Trowe, T., Karlstrom, R.O., Nüsslein-Volhard, C., and Bonhoeffer, F. (1996). Genetic dissection of the retinotectal projection. *Development* *123*, 415–425.
30. Trowe, T., Klostermann, S., Baier, H., Granato, M., Crawford, A.D., Grunewald, B., Hoffmann, H., Karlstrom, R.O., Meyer, S.U., Müller, B., et al. (1996). Mutations disrupting the ordering and topographic mapping of axons in the retinotectal projection of the zebrafish, *Danio rerio*. *Development* *123*, 439–450.
31. Gallego, J.A., Perich, M.G., Chowdhury, R.H., Solla, S.A., and Miller, L.E. (2020). Long-term stability of cortical population dynamics underlying consistent behavior. *Nat. Neurosci.* *23*, 260–270.
32. Stefanini, F., Kushnir, L., Jimenez, J.C., Jennings, J.H., Woods, N.I., Stuber, G.D., Kheirbek, M.A., Hen, R., and Fusi, S. (2020). A distributed neural code in the dentate gyrus and in CA1. *Neuron* *107*, 703–716.e4.
33. Baumann, O., Borra, R.J., Bower, J.M., Cullen, K.E., Habas, C., Ivry, R.B., Leggio, M., Mattingley, J.B., Molinari, M., Moulton, E.A., et al. (2015). Consensus paper: the role of the cerebellum in perceptual processes. *Cerebellum* *14*, 197–220.
34. Bird, C.M., Berens, S.C., Horner, A.J., and Franklin, A. (2014). Categorical encoding of color in the brain. *Proc. Natl. Acad. Sci. USA* *111*, 4590–4595.
35. Nambodiri, V.M.K., Rodriguez-Romaguera, J., and Stuber, G.D. (2016). The habenula. *Curr. Biol.* *26*, R873–R877.
36. Lin, Q., and Jesuthasan, S. (2017). Masking of a circadian behavior in larval zebrafish involves the thalamo-habenula pathway. *Sci. Rep.* *7*, 4104.
37. Dreosti, E., Vendrell Llopis, N., Carl, M., Yaksi, E., and Wilson, S.W. (2014). Left-right asymmetry is required for the habenulae to respond to both visual and olfactory stimuli. *Curr. Biol.* *24*, 440–445.
38. Clark, D.T. (1981). Visual responses in developing zebrafish (*Brachydanio rerio*) (University of Oregon), PhD thesis.
39. Burgess, H.A., and Granato, M. (2007). Modulation of locomotor activity in larval zebrafish during light adaptation. *J. Exp. Biol.* *210*, 2526–2539.
40. Valente, A., Huang, K.-H., Portugues, R., and Engert, F. (2012). Ontogeny of classical and operant learning behaviors in zebrafish. *Learn. Mem.* *19*, 170–177.
41. Yashina, K., Tejero-Cantero, Á., Herz, A., and Baier, H. (2019). Zebrafish exploit visual cues and geometric relationships to form a spatial memory. *iScience* *19*, 119–134.
42. Nevin, L.M., Robles, E., Baier, H., and Scott, E.K. (2010). Focusing on optic tectum circuitry through the lens of genetics. *BMC Biol.* *8*, 126.
43. Avitan, L., Pujic, Z., Mölter, J., Van De Poll, M., Sun, B., Teng, H., Amor, R., Scott, E.K., and Goodhill, G.J. (2017). Spontaneous activity in the zebrafish tectum reorganizes over development and is influenced by visual experience. *Curr. Biol.* *27*, 2407–2419.e4.
44. Guggiana-Nilo, D.A., and Engert, F. (2016). Properties of the visible light phototaxis and UV avoidance behaviors in the larval zebrafish. *Front. Behav. Neurosci.* *10*, 160.
45. Orger, M.B., and Baier, H. (2005). Channeling of red and green cone inputs to the zebrafish optomotor response. *Vis. Neurosci.* *22*, 275–281.
46. Conway, B.R., Eskew, R.T., Jr., Martin, P.R., and Stockman, A. (2018). A tour of contemporary color vision research. *Vision Res.* *151*, 2–6.

47. Liu, Y., Li, M., Zhang, X., Lu, Y., Gong, H., Yin, J., Chen, Z., Qian, L., Yang, Y., Andolina, I.M., et al. (2020). Hierarchical representation for chromatic processing across macaque V1, V2, and V4. *Neuron* 108, 538–550.e5.
48. Ben Fredj, N., Hammond, S., Otsuna, H., Chien, C.-B., Burrone, J., and Meyer, M.P. (2010). Synaptic activity and activity-dependent competition regulates axon arbor maturation, growth arrest, and territory in the retinotectal projection. *J. Neurosci.* 30, 10939–10951.
49. Maddison, L.A., Lu, J., Victoroff, T., Scott, E., Baier, H., and Chen, W. (2009). A gain-of-function screen in zebrafish identifies a guanylate cyclase with a role in neuronal degeneration. *Mol. Genet. Genomics* 281, 551–563.
50. Freeman, J., Vladimirov, N., Kawashima, T., Mu, Y., Sofroniew, N.J., Bennett, D.V., Rosen, J., Yang, C.-T., Looger, L.L., and Ahrens, M.B. (2014). Mapping brain activity at scale with cluster computing. *Nat. Methods* 11, 941–950.
51. Vladimirov, N., Mu, Y., Kawashima, T., Bennett, D.V., Yang, C.-T., Looger, L.L., Keller, P.J., Freeman, J., and Ahrens, M.B. (2014). Light-sheet functional imaging in fictively behaving zebrafish. *Nat. Methods* 11, 883–884.
52. Schneider, C.A., Rasband, W.S., and Eliceiri, K.W. (2012). NIH Image to ImageJ: 25 years of image analysis. *Nat. Methods* 9, 671–675.
53. Rohlfing, T., and Maurer, C.R., Jr. (2003). Nonrigid image registration in shared-memory multiprocessor environments with application to brains, breasts, and bees. *IEEE Trans. Inf. Technol. Biomed.* 7, 16–25.
54. Baden, T., Berens, P., Franke, K., Román Rosón, M., Bethge, M., and Euler, T. (2016). The functional diversity of retinal ganglion cells in the mouse. *Nature* 529, 345–350.
55. Sjöstrand, K., Clemmensen, L.H., Larsen, R., Einarsson, G., and Ersbøll, B. (2018). SpaSM: a MATLAB toolbox for sparse statistical modeling. *J. Stat. Softw.* 84, <https://doi.org/10.18637/jss.v084.i10>.
56. Meehan, C., Meehan, S., and Moore, W. (2020). Uniform Manifold Approximation and Projection (UMAP) (MATLAB Central File Exchange).

STAR★METHODS

KEY RESOURCES TABLE

REAGENT or RESOURCE	SOURCE	IDENTIFIER
Deposited data		
Extracted ROIs	This paper	https://dx.doi.org/10.17632/szj869h34m.1
Experimental models: organisms/strains		
Zebrafish: Tg(ath5:Synaptophysin-GCaMP6s, isl3:Synaptophysin-GCaMP6s)	48,49 and this paper	N/A
Zebrafish: Tg(HuC-H2B:GCaMP6s)	50	N/A
Zebrafish: Tg(HuC:GCaMP6s)	51	N/A
Software and algorithms		
Custom MATLAB code for data analysis	Mathworks, this paper	https://www.mathworks.com/ , https://github.com/drguggiana/Guggiana_2021
Custom LabVIEW code for microscope control and stimulus generation	National Instruments, this paper	https://www.ni.com/
ImageJ	52	https://imagej.nih.gov/ij/index.html
Cygwin	https://www.cygwin.com/	https://www.cygwin.com/
CMTK	53	https://www.nitrc.org/projects/cmtk/

RESOURCE AVAILABILITY

Lead contact

Further information and requests for resources and reagents should be directed to and will be fulfilled by the Lead Contact, Dr. Drago Guggiana Nilo (drguggiana@neuro.mpg.de).

Materials availability

This study did not generate new unique reagents.

Data and code availability

Original data have been deposited to Mendeley Data: <https://dx.doi.org/10.17632/szj869h34m.1> and the code generated is available on Github at https://github.com/drguggiana/Guggiana_2021.

EXPERIMENTAL MODEL AND SUBJECT DETAILS

Zebrafish

5-7 days post fertilization (dpf) male and female zebrafish larvae (*Danio rerio*, Hamilton, 1822, sex not identifiable at this age) were group bred in a 14:10 light/dark cycle at 28°C in 10 cm dishes. The strains used were 1) Tg(ath5:Synaptophysin-GCaMP6s, isl3:Synaptophysin-GCaMP6s),^{48,49} 2) Tg(HuC-H2B:GCaMP6s)⁵⁰ and 3) Tg(HuC:GCaMP6s),⁵¹ all in a *nac*^{-/-} background (RRID:ZFIN_ZDB-GENO-990423-18). 1) expresses GCaMP6s at the axonal terminals of most RGCs in the larval zebrafish, 2) expresses the same calcium indicator localized to the nuclei of most neurons in the larval brain, and 3) expresses also the same calcium indicator in the cell body of most neurons across the whole brain. All animal protocols were in accordance with NIH guidelines and the Harvard University IACUC.

METHOD DETAILS

Stimulus presentation

The larvae were embedded in 1.8% agarose (UltraPure Low Melting Point Agarose, 16520-100, Invitrogen) in a 5 cm plastic Petri dish that was then filled with filtered facility water. The stimuli were presented using a custom-built four channel projector. Briefly, two Lightcrafter projectors (Lightcrafter Evaluation Module, Texas Instruments, Dallas, TX, USA) were stacked on top of each other. One of them was modified to support projection of LEDs centered at 606, 463 and 397 nm by changing the dichroic mirrors in the light engine. The second projector was stripped of its dichroic mirrors and the focusing lens was replaced by one supporting UV

transmission (354330-A, $f = 3.1$ mm, NA = 0.68, Unmounted Geltech Aspheric Lens, Thorlabs Inc., Newton, NJ, USA). Then, a UV LED (365nm, Mouser Electronics, Mansfield, TX, USA) was mounted at the entrance port of the former red LED. The two projectors were coupled using a flat mirror and a dichroic mirror (PF20-03-F01, Thorlabs Inc.) and their projections were aligned underneath the animal. All stimuli were synthesized by custom software written in LabVIEW (National Instruments, Woburn, MA, USA).

Brain imaging

Two photon calcium imaging was performed using a custom built point scanning two-photon microscope. Briefly, a Mai-Tai femto-second laser tuned to 950 nm was passed through a computer controlled half-wave plate and a polarization sensitive prism. After the prism, the beam was expanded to 5 mm and delivered to the center of a set of scanning galvanometric mirrors (Cambridge Technology, Cambridge, MA). The objective used was an Olympus 20X XLUMPLFN-W water immersion objective (Olympus Corporation, Shinjuku, Tokyo, Japan). Light collected from the sample was relayed to a dichroic mirror that then diverted it to a gateable photomultiplier tube (H11526, Hamamatsu Photonics K.K.), after bandpassing by a filter (Chroma, Bellows Falls, VT). Additionally in the path, there was a Hitachi camera focused on the sample plane to allow for rough sample positioning. The microscope control software was written in LabVIEW (National Instruments, Woburn, MA, USA). The entire system was synchronized so that the stimulus was presented only during the turn around and fly-back periods of the mirror, at which point the PMT was gated off, therefore preventing direct exposure from the projector light. This is important, as green light stimulation travels unimpeded through the optical path to the PMT given the emission wavelength of GCaMP. Images were acquired at ~ 1 -2 frames per second, at a resolution of 320x320 pixels. Each trial was 40 s in length with 10 s of adaptation, 20 s of stimulus presentation and 10 s of rest before the next trial. All stimuli were shown in triplicate to each animal before moving onto the next z section and repeating the whole process. The stimuli presented for [Figures 1, 2, and 3](#) were full field, single LED intensity oscillations following a sinusoidal temporal structure (0.25 cycles/s, maximum intensity swing, [Figure S1A](#)). During the rest before and after the stimulus, the intensity of the selected LED was left constant and at medium level. For [Figure 4](#), the stimuli were of 3 types: a full field checkerboard with either red or UV in half of the squares and black in the others, oscillating sinusoidally in intensity during the stimulation period and remaining static during the rest periods. The second stimulus was a moving grating alternating the red or UV light with black stripes. The grating was static during rest periods and moved from caudal to nasal during the stimulation period at a spatial frequency of 1cm/cycle and a temporal frequency of 1 cycle/s. The third stimulus was a full field red or UV light that suddenly reduced in intensity to 0 for a single frame (900 ms) 20 s after the start of the stimulus, and then returned to its original intensity for another 20 s. For the RA population the targets were the optic tectum, pretectum, habenula, and cerebellum. For the RGC population the targets were AF4-10, although no signals were found in AF7 and 6 as noted in the text. AF1-3 were not included in our protocol, as their deep location close to the eye was impractical for our microscope and would have resulted in exceedingly long experiments.

Data pre-processing

The raw data followed a pre-processing pipeline that has been described previously.⁴ Briefly, the raw imaging data were imported into MATLAB (Mathworks, Natick, MA, USA), and all frames within a z section were aligned based on their cross correlation from time point to time point. Following alignment, the $\Delta F/F$ was calculated for each stimulus repetition, and the repetitions were collapsed into an average. With the repetitions condensed, all the frames corresponding to one z plane were concatenated and the correlation of each voxel with its 8 neighbors within a plane was calculated across time. An iterative algorithm was used to find the highest correlation value in each z plane and then start grouping it with its neighbors based on a correlation threshold, up to a size threshold or until there were no more neighbors fulfilling the correlation threshold. This was repeated for each high correlation value to yield several groups of voxels. These small groups of voxels, termed ROIs, were then used as the unit to generate each one of the calcium traces used in the study. To obtain each trace, the traces from each voxel in an ROI were averaged together. Finally, signal to noise ratio per stimulus was approximated as described in [Baden et al.](#)⁵⁴ by taking the ratio of the averaged standard deviation across repetitions for each trace, and the standard deviation of the average. Then traces below the 25th percentile for all stimuli were excluded from the analysis (around 10% of the traces).

Since the ROI extraction in RGC axonal terminals suffers from resolution constraints, given the size of the terminals, potential effects of this were probed. In particular, the RA dataset was artificially spatially downsampled to approximately match the resolution of ROIs in the RGC dataset (downsampling factor of 3), and then ROIs with the same parameters as for the RGC dataset were extracted. The spectral polarities and response clusters ([Figures S1H and S2G](#)) were compared to the original data. Although some important distortions are observed as expected, the main spectral polarities and clusters are present in both cases.

To account for the differences in dynamics between the axonally expressed GCaMP6s in RGCs compared to the somatically expressed GCaMP6s in RAs, two methodologies were attempted. In the first one, the spectral polarities and the clusters obtained from our RA dataset were compared with a dataset obtained from a nuclearly localized GCaMP6s also expressed in RAs, which should be even slower than the somatic GCaMP ([Figures S1F and S2F](#)). The second method was to obtain the average calcium response of the RGC and RA data. Then convolution was used to artificially “delay” the RGC data to match the RA data (decay constant 0.2), and compare spectral polarities and clusters ([Figures S1G and S2H](#)). Both methods showed that most spectral polarities and clusters are recovered under the manipulations.

Calculation of cone gains

This first approximation was calculated assuming linearity in the signal summation from different cone types following Equation 1.

$$(I_1 I_2 I_3 I_4) \begin{bmatrix} W_1 C_{11} & W_1 C_{21} & W_1 C_{31} & W_1 C_{41} \\ W_2 C_{12} & W_2 C_{22} & W_2 C_{32} & W_2 C_{42} \\ W_3 C_{13} & W_3 C_{23} & W_3 C_{33} & W_3 C_{43} \\ W_4 C_{14} & W_4 C_{24} & W_4 C_{34} & W_4 C_{44} \end{bmatrix} = (E_1 E_2 E_3 E_4) \quad (\text{Equation 1})$$

Namely, that a linear combination of the contributions from each cone type (C_{ij}), weighted by constant factors considering the cone and LED spectra (W_i), is able to explain the observed responses (E_j) as a function of LED intensity (I_j). To perform this analysis, the Fourier transform of the traces was extracted to obtain the power at the frequency of stimulation (0.125 Hz). This power was used as the value for the response to each LED. Then, an interaction matrix was constructed, containing the expected excitation of each cone type based on the cone spectra, the LED spectra and the power of the LED. The key element is that, for each stimulus, each LED is turned on on its own, and hence the entire relationship reduces to a four-equation, four-unknown system that can be solved exactly (Equation 2). This yielded a set of cone "gains" for each trace.

$$\begin{aligned} I_1 W_1 C_{11} &= E_1 \\ I_2 W_2 C_{22} &= E_2 \\ I_3 W_3 C_{33} &= E_3 \\ I_4 W_4 C_{44} &= E_4 \end{aligned} \quad (\text{Equation 2})$$

Gain pattern classification

For identifying the color input patterns into the ROIs evaluated in this study, the cone gain patterns were simplified analogous to the procedure described in Zhou, Bear et al.⁸ Namely, the gains within the lowest percentile of average response (10th in our case) were set to 0, and then any gain with a positive value was assigned a 1 and every gain with a negative value was assigned a -1. Then, the unique patterns present in the data were identified and their occurrences counted. For plotting, the same color convention as described in the reference above was used, namely, black signifies OFF, white signifies 0 and any given color signifies ON. For the comparison data in Figure S1C, the publicly available dataset from Zhou, Bear et al. was downloaded, and only the dorsal retina data were selected (between 1 and 3.5 in the horizontal axis of the unfolded retina). Finally, the processing steps described in the reference were followed to obtain the RGC types.

Registration

The registration procedure was a modification from the one described in Randlett et al.²⁸ Briefly, the average stacks of images for each animal and experiment were Gaussian blurred and converted to nrrd format, including the metadata for pixel size, and oriented the same as the reference brain (nasal up, all using ImageJ⁵²). Then, the software CMTK (Computational Morphometry Toolkit, <http://nitrc.org/projects/cmtk>⁵³) was utilized to register them in three dimensions to a reference brain, which varied depending on the dataset. The reference brain was cut so as to better match the imaged volume, and hence facilitate the registration process. For the registration itself we used the munge wrapper for CMTK with the following command line parameters: -a -r 01 -l a -v -T 8 -X 52 -C 4 -G 5 -A '-accuracy 0.4' for the isl2 reference brain and (isl3+ath5)::synaptophysin-GCaMP6s data, and -a -r 01 -l a -v -T 8 -X 52 -C 8 -G 20 -A '-accuracy 0.4' for the HuC reference brain and corresponding HuC::GCaMP6s and HuC::H2B-GCaMP6s data. Once registered, the affine matrix was loaded into MATLAB and the registration parameters were applied to the raw calcium data. These coordinates were translated from the cut reference brains to the original, full-size reference brains, so as to make them compatible with the full Z Brain Atlas. To produce the maps displayed in the manuscript, after reformatting of the ROIs, the average across the stimulation period for each ROI was calculated. Then, the 75th percentile across all ROIs for each stimulus was calculated, and only the ROIs above this threshold were kept. After that, the signal from all ROIs that crossed the threshold was added in space and was superimposed on the reference brain stack after normalization of both. Finally, to generate the display maps in Figures 1G, 2D, and 4D, the maximum intensity projection in z was calculated. For the statistical comparison in Figures 1J and S1D, each maximally projected profile was divided in 5 sections, and the corresponding sections were compared across stimuli.

Similarity index

To obtain a measure of the overlap between the anatomical location of the responding ROIs for each stimulus, the ROIs were thresholded based on the top 75th percentile of response. Then, a Gaussian blurring filter was applied to the position of each remaining ROI to account for the inaccuracies in registration, and next the overlap between the ROI sets from each stimulus (when positioned in the reference brain on a trial by trial basis) was calculated. The overlap was quantified as the number of voxels that coincided between the ROIs from each stimulus, without taking intensity into account as this is accounted for by the percentile threshold. To normalize the cross stimulus overlap, the overlap between single trials of the same stimulus was calculated, and then the cross-stimulus overlap was divided by the average of the within stimulus overlap for the pair of stimuli in question, thus resulting in a similarity index that is then plotted in Figures 1K and 4E for their respective datasets.

Dimensionality reduction and clustering

Given the high dimensionality of the data, the traces were processed using the method described in Baden et al.⁵⁴ Sparse principal component analysis (via the SpaSM MATLAB package by Sjöstrand et al.⁵⁵) was used to reduce the dimensionality of each trace. In

particular, 4 sPCs were used per stimulus, each one with 10 active bins. To find the ideal number of clusters, the analysis was performed with several cluster numbers and then the one with the minimum Bayesian Information Criterion value was selected. This criterion balances the increase in fit from a stronger model with a penalty to the complexity of the model. The entire process was performed using the Expectation Maximization algorithm in MATLAB to fit a Gaussian Mixture Model to the data. Finally, clusters with a correlation higher than 0.8 were merged due to their similarity.

UMAP

Uniform Manifold Approximation and Projection analysis was performed on the stimulus period of the neural data at the population level. This was done separately for the AF10-Tectum 4 color dataset and AF10-Tectum 2 color dataset. We used the implementation for MATLAB written by Meehan et al.⁵⁶ The calcium data were projected into PCA space using the sparse principal components used for clustering, normalized, and then processed with the UMAP software. Finally, the 75th percentile of the responses was calculated, and the ROIs were colored based on this number per stimulus to generate [Figures S3D](#) and [S4D](#).

SVM color and intensity classification

To perform the Support Vector Machine classification, the data were supplied to the `fitcecoc` function in MATLAB, which trains a series of binary SVM classifiers to perform multi-class classification. The structure of the binary classifiers is a one-versus-all arrangement, where each binary classifier is trained to separate one category from all the rest (which comprise a single “negative” category together). Then the points that score the highest for a given category are assigned to that one. The classifier for [Figures 2E](#) and [S2J](#) was trained to separate between the four sinusoidal stimuli (i.e., four categories) on a per region basis. One classifier was trained per fish, using only the stimulus period binned to four bins and 5-fold cross validation. The MATLAB function `kfoldpredict` was used to obtain the performance for classifying the left out samples in each separate classifier and these were averaged to obtain the classification per fish. Performance of the classifier was assessed as the average percentage of the traces across the diagonal of the confusion matrix (diagram comparing the delivered versus predicted stimulus), either on a per row basis (per stimulus performance) or averaging the whole diagonal (overall performance). The performances of all fish were then averaged to obtain an overall performance, and the whole process was repeated ten times. The control classification used the same process, but the labels for the four stimuli were pseudorandomized. For the intensity classifier in [Figure S2K](#), we utilized the same procedure outlined above, but instead of using one label per stimulus, we used five levels per stimulus, one for each of the intensity levels of the LED during that stimulus.

The classifiers in [Figures S1F–S1H](#) (bottom) were calculated as for [Figure 2E](#), but compared the RA data to either the H2B ([Figure S1F](#)), the delayed RGC data ([Figure S1G](#)) or the spatially downsampled RA data ([Figure S1H](#)). All classifiers were trained using random subsampling to match ROI numbers.

ROI addition analysis

The ROIs for a given dataset and fish were ranked based on their contribution to the classifier. In particular, an importance index was calculated as defined in Stefanini et al.³² Briefly, since the multiclass classifier relies on a series of binary classifiers, to assess the relevance of an individual ROI in the overall classification, the absolute values of the weights are calculated and then averaged across binary classifiers and across folds. This index was used to train classifiers starting with the weakest ROIs and progressively training classifiers with more ROIs in ascending order of relevance. The goal is to determine how distributed or local the neural code is based on the shape of the curve, and how it compares between neural populations. This cycle was repeated 10 times for each classifier. This analysis was utilized to generate [Figures 3J](#) and [4G](#).

Success ratio

To quantify the reliability of the classifier over time while taking into account its high performance, a success ratio was calculated as follows. The subtraction of the correctly classified frames and the incorrect ones was divided by the total number of frames. This value was calculated for every classifier separately and averaged for display in [Figure 3I](#).

Cluster to cluster regression

As an alternative way to assess the similarity between the responses in each region, the average of each cluster per region was calculated, and then cross-validated linear regression was used to fit the responses of one region with another. This was done for all the possible pairings of regions. Then, for each pair, the losses from the fits to each cluster were averaged and saved in a matrix. Finally, the results were plotted in [Figure S2C](#) as one minus the average loss, since we wanted a measure of similarity.

Correlation analysis

Four different types of (de)correlation were calculated, all using Pearson’s correlation coefficient and only the stimulus period (excluding pre- and post-stimulus), except for [Figures S3A](#) and [S3B](#) that used the whole period. For calculation of the decorrelation matrices in [Figure 3D](#), the datasets were reshaped so that all of the responses for a given stimulus are concatenated across neurons, and separated by stimulus. Then a correlation matrix was calculated based on this input so that the result had the dimensions of the number of stimuli. Decorrelation was calculated as one minus the absolute value of the correlation, since the quantity of interest is decorrelation, not the positive and negative nature of the correlations. This was done with both the four sinusoidal stimuli dataset and the red/UV pattern dataset. To calculate the decorrelations shown in [Figure 3E](#), the cluster averages from the responses for the

different stimuli within a brain region (AF10 or tectum) were correlated against each other, yielding a pairwise correlation matrix of color comparisons for that brain region. Decorrelation was calculated as described for [Figure 3D](#). For calculation of the stimulus-to-stimulus correlation over time in [Figures S3A](#) and [S3B](#), the traces were concatenated across neurons, but they were kept separate for each time point. Then, the traces for each stimulus were correlated with each other at each time point, yielding the trajectories displayed. All of the above computations were performed individually per animal and then averaged. For calculation of the fish correlations, the data from all the animals in the tectal dataset was clustered together, then the traces from each animal were averaged based on their belonging to a cluster. These averages were then correlated across animals and an average correlation per individual was calculated and displayed in [Figure S2D](#).

PCA-CCA

Principal Component Analysis was performed separately for each animal, using the neural response data for the stimulus period only. As outlined in Gallego et al.,³¹ although PCA realigns the space the data are in uniquely for that data (i.e., set of neurons/axonal terminals), if the underlying variance-driving dimensions are similar, or in other words if the sets of responses from different animals lie in the same manifold of activity, one can use Canonical Correlation Analysis to find a common subspace that maximizes the alignment between the PCA reconstructions from different sets of ROIs. Therefore this technique was utilized to align the PCA decompositions of the stimulus responses for the AF10 and tectum from different animals. Only the animals that had at least three dimensions containing 50% (4-color stimulus set) or 80% (2-color stimulus set) of the variance or higher were considered (3 animals for the AF10 population and 5 animals for the tectal population). These trajectories were then averaged to generate the displays shown in [Figure 3F](#). These aligned trajectories were also used to compute the results in [Figure 3G](#).

Convolution of chromatic kernels

The dataset from Zhou, Bear et al. was downloaded from the published repository and the chromatic kernels for each ROI were extracted using the provided code. These kernels were then convolved with the waveforms representing the stimuli used in this study after matching time bases. This produced a set of traces that was processed using the pipeline developed in this study to obtain spectral types and clusters. The spectral types were compared with the types reported in the Zhou, Bear et al. study ([Figure S1C](#)), and the clusters were compared to the ones obtained from using the Gaussian Mixture Model produced in this study, but the kernel-derived traces ([Figure S2I](#)).

QUANTIFICATION AND STATISTICAL ANALYSIS

All statistical analyses were performed in MATLAB. For all quantifications non-parametric statistical tests were utilized: either the Wilcoxon Rank Sum, Wilcoxon Signed Rank or permutation tests as indicated in the main text or figure legends. The significance level was defined as 0.05 for all tests. The center measures utilized were mean and median (when appropriate) and the dispersion measure was the standard error of the mean. “n” is defined as the number of larvae or the number of ROIs, with clear indication of which of the two it corresponds to in the text and figures throughout the manuscript. No methods were utilized to determine whether the data met the assumptions of the statistical approach, as no parametric methods were used. For [Figures 1J](#), [1K](#), [3E](#), [3G](#), [4E](#), and [S1D](#), we corrected for multiple comparisons across the different stimuli (6 possible comparisons) using the Bonferroni method to adjust the p value accordingly. All other tests were performed pairwise once.